

Diagnostics & Applications: The He I 5876 Å Transition in a Solar Prominence

Ross MacDonald

*Supervisor: Dr. Nicolas Labrosse
The Astronomy & Astrophysics Group,
The School of Physics & Astronomy,
University of Glasgow*

September 4, 2020

Abstract

A solar prominence is a phenomenon which influences more than the regions it engulfs, with the effects of an eruptive prominence felt across the solar system. Due to our limited understanding of prominence structures caused by the difficulty of capturing these events, a new system of space-based coronagraphs must be deployed. These will equip researchers with continuous observational data, as opposed to limited data of specific events. The He I 5876 Å transition (also known as the D₃ transition) is the ideal candidate for advancing prominence research, as it is detectable within the visible range of the electromagnetic spectrum, whilst providing a wealth of diagnostic information on the magnetic field structure of a prominence via spectropolarimetry. Continuous analysis of this line within prominence structures will have long standing benefits in fields of research such as space weather patterns.

Due to launch in 2022, PROBA-3¹ will carry ASPIICS² and provide year-round coverage of solar prominence events. Presently, ASPIICS will integrate white light centred around a 20 Å passband. It is key that the diagnostic potential of the D₃ line is realised before launch to maximise its potential. The results from this project could also be extended and applied to METIS³, launched on-board Solar Orbiter in early 2020.

Using the C2D2E radiative transfer code, which models 2D cylindrical prominence structures, this project will analyse the results from a range of different models. For models which include a prominence to corona transition region (PCTR), the helium abundance ratio of the prominence and the cylindrical radius are varied at an altitude of 10,000 *km* to analyse various forms of the emission measure as a function of the integrated intensity of the D₃ line, alongside the associated contribution function for selected models. For models which do not include a PCTR, the helium abundance ratio, cylindrical radius and gas pressure are altered, in order to plot the integrated

¹PROBA - Project for On-Board Autonomy

²ASPIICS - Association of Spacecraft for Polarimetric and Imaging Investigation of the Corona of the Sun

³Multi-Element Telescope for Imaging and Spectroscopy

intensity of the D_3 emission as a function of temperature.

This project concludes that, for models with a PTCR, the electron-singly-ionized helium emission measure continues to display a linear relationship when plotted as a function of the integrated intensity of the D_3 line. In addition, the contribution functions display a strong ring structure, showing that the PTCR is affecting the D_3 emissions from the line formation at the centre of the prominence. This also presents the possibility that D_3 line formation does occur in the PCTR. For the models with no PTCR, it was found that 2D simulations produce a larger integrated intensity of the D_3 emission than the corresponding 1D simulations.

Acknowledgements

First, I'd like to acknowledge the team I had the pleasure of working in over the summer of 2020. Without the help, guidance and ideas from my supervisor, Dr. Nicolas Labrosse, this project would simply not have been possible. In addition, the help and advice from Dr. Sargam Mulay, Aaron Peat and Chris Osbourne had a huge impact on the outcome of my project. Finally, I'd like to thank my fellow summer students for the various discussions and ideas during our meetings, namely Arihant Changkakati, Matthew Docherty, Naomi Shakespeare-Rees and Pakawee Surarittikul.

Completing a masters course was an exciting but daunting task, as it more-or-less signals the end of my time as a taught student. It also offers a time to reflect on my career in physics so far, and how small exchanges and influences helped shape the path I took. I'd like to thank my old lecturers from the University of the West of Scotland, namely Dr. David Hutson, Dr. Alan Walker, Professor Marcus Scheck and Dr. David O'Donnell amongst the other members of the faculty.

On a personal level, it is important to acknowledge the friendships which helped drive me forward during the past five years. Namely, Dion Blackburn, Amy Carroll, Connor Douglas, Ross Johnston, Greig Oliver, Paolo Sassarini and Andrew Scott. Finally, if it wasn't for some harsh truths shared in my first year of university, I would not have made it this far. Paul Docherty and Tony Vinnicombe provided career advice in the space of two minutes which proved to be invaluable, proving that small conversations and acknowledging the truth can have profound effects on the years ahead.

Contents

List of Figures	vi
List of Tables	vii
1 The Prominence of Prominences: An Introduction to Solar Prominence Research	1
2 Theory	9
2.1 The Basics of a Solar Prominence	9
2.2 Radiative Transfer Modelling	11
2.2.1 Basic Radiative Transfer	11
2.2.2 C2D2E Radiative Transfer & Statistical Equilibrium	12
2.2.3 Spectral Line Formation Mechanisms	15
2.3 Wider Applications	16
2.3.1 Space Instruments	16
2.3.2 Magnetic Field Inference	17
3 Methodology	20
3.1 C2D2E Routines & Calculations	20
3.2 The Models Used	21
4 Results	26
4.1 Altering the Helium Abundance Ratio	26
4.2 Altering the Cylindrical Radius	29
4.3 Integrated Intensity of the D ₃ Emission as a Function of Temperature	31
5 Conclusions	35

6	Appendix	38
6.1	D3 Contribution Function & 584 Å Contribution Function	38
7	Bibliography	40

List of Figures

1.1	A diagram of the model used by Labrosse and Gouttebroze in 2001.	2
1.2	The geometry used in Gouttebroze & Labrosse (2009).	4
1.3	Emission measure results for 2D radiative transfer simulations.	5
1.4	Results from 1D simulations plotting integrated intensity against temperature. .	7
1.5	The results of integrated intensity ($D_3 + VL$) against temperature.	7
2.1	An eruptive quiescent prominence observed by the Solar Dynamics Observatory on the 31st of August 2012.	10
2.2	Transition diagram for C2D2E.	15
4.1	The emission measure as a function of D_3 intensity from models changing the helium abundance ratio.	27
4.2	The contribution function for models which altered the helium abundance ratio.	28
4.3	The emission measure as a function of D_3 intensity for models altering the cylin- drical radius.	29
4.4	The contribution function for PCTR models altering the cylindrical radius. . . .	30
4.5	Integrated intensity as a function of temperature for models with a different gas pressure.	31
4.6	Integrated intensity as a function of temperature for models altering the helium abundance ratio and the cylindrical radius.	33
6.1	Contribution Function plotting the evolution of the intensity from the D_3 and 584 Å abundance ratio models.	38
6.2	Contribution Function plotting the evolution of the intensity of the D_3 and 584 Å from models altering the cylindrical radius.	39

List of Tables

3.1	Models used which included a PCTR.	22
3.2	Models which altered the helium abundance ratio with no PCTR present.	23
3.3	Models altering the gas pressure with no PCTR present.	24
3.4	Models altering the cylindrical radius with no PCTR present.	25

Chapter 1

The Prominence of Prominences: An Introduction to Solar Prominence Research

As our closest star, the sun provides the perfect opportunity for extensive research into the power sources of the universe. By understanding our star, that knowledge can then be applied to distant stars, aiding in our understanding of how the solar system, galaxies and the universe operates. This project will consider quiescent solar prominences, which are large magnetic structures originating from the depths of the sun and extending a region of (relatively) cool plasma into the hot solar corona. Throughout many years of observations and computational simulations, the neutral Helium transition, He I 5876 Å (D₃), has emerged as a key transition to extract diagnostic information from a prominence. Two main approaches have been employed: radiative transfer modelling, and spectropolarimetry, both of which can be used to infer the magnetic field structure of a prominence. This section details the history and ideas behind the radiative transfer model being used [14] alongside comparisons with a competing model [21].

Much of the current research using modelling techniques to simulate solar prominence events can be traced back to the work of Gouttebroze, Heinzel and Vail (GHV) in 1993 [12]. In this, they computed the theoretical emissions of a hydrogen atom in a solar prominence. To do so, the statistical equilibrium and radiative transfer equations were solved for a 2-level hydrogen atom, modelling the prominence as 2D plane-parallel slabs under isothermal and isobaric conditions. In their simulations, they ran 140 models, which were each identifiable by three parameters:

kinetic temperature; gas pressure; and the thickness of the slab. The micro-turbulent velocity was set to 5 km s^{-1} , and the height above the solar surface was set to $10,000 \text{ km}$. The results were extensive, including the proposal that comparison of the integrated intensities of emission lines provided information about the conditions in which the emission line was formed. However, they concluded that this code was merely the foundations on which to build future models, as opposed to their model forming a complete picture of the solar spectrum in a prominence.

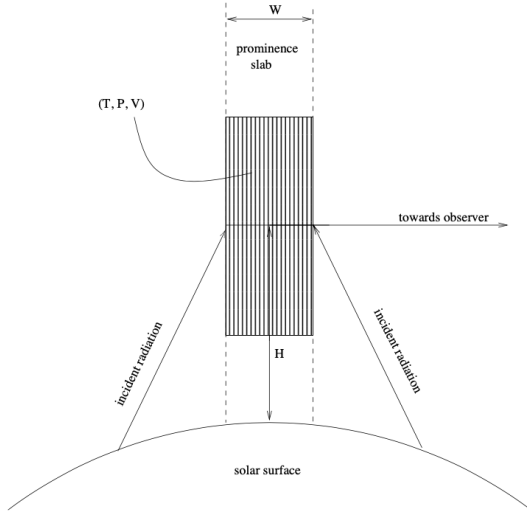


Figure 1.1: A diagram of the model used by Labrosse and Gouttebroze in 2001. The variables T , P and V represent the gas temperature, gas pressure and micro-turbulent velocity respectively, W is the width of the prominence slab, and H is the height of the structure above the solar surface [17].

creases, the optical thickness will decrease. One issue with the code is that it merely focused on hydrogen, meaning more work had to be done to form a more accurate picture of prominence events, such as the inclusion of helium.

In 2001, Labrosse and Gouttebroze published a model which simulated helium in solar prominences [17]. Due to previous models having only dealt with hydrogen simulations, this was an important step forward as it included better atomic models and dealt with incident radiation with an increased accuracy. Helium must be an essential part of any realistic simulation due to its abundance, making up around 23.8% of the mass of the solar atmosphere [22]. The technique

In 2000, Gouttebroze and Labrosse revised the GHV code, expanding on the ideas presented [13]. This paper used the same technique of plane-parallel slabs under isobaric and isothermal conditions but broadened the conditions which defined the models. Whereas GHV only had three identifiable parameters, this paper increased it to five with the addition of the micro-turbulent velocity and the height of the structure above the solar surface. Because this paper was an update to the code rather than reporting new findings, only one example result was given to illustrate its application. This result showed the evolution of the $L\alpha$ hydrogen line throughout the prominence slabs. The conclusion was that the slab displayed optically thick behaviour at the bottom, whereas the top was optically thin, suggesting that as the temperature increases and the pressure decreases,

was the same as used in the 2000 paper by the same authors, with the idea of plane-parallel slabs shown in figure 1.1. Various situations were examined, looking for any change in the emission spectrum by altering the slab width, temperature, gas pressure, or the helium abundance ratio. Briefly summarising the results, altering the slab width caused the intensity of the D_3 line to vary. Additionally, the integrated intensity over several wavelengths (from the 304 Å to 6678 Å) for five different temperatures (6000 K to 20,000 K) as a function of slab width starts in the same ballpark for a small slab width (10^2 km), but vastly increases in diversity for larger slab widths (10^5 km). With regards to temperature, keeping gas pressure constant and increasing the temperature shows an increase in intensity. They then compared the mean level populations between two pressures as a function of the temperature. The D_3 line is an optically thin triplet transition between $1s2p\ ^3P$ and $1s3d\ ^3D$, and these levels show similar behaviours during the simulation. This showed that the level populations which lead to optically thin transitions are mostly affected by thermal processes, causing the line intensity to increase in high temperature scenarios. When analysing the relationships between lines, they found that the D_3 emission and the 10830 Å have a linear relationship, with this only changing when the 10830 Å line became optically thick. This finding hints at the diagnostic potential of the 10830 Å line alongside D_3 , as any change in one integrated intensity will also occur for the other line. Echoing this statement in their conclusions, they observed that the relationship between line intensities could be used to improve their simulations of helium in a prominence and proposed doing the same for hydrogen. However, they acknowledged that this simulation did not form a complete picture, as improvements could be made by the inclusion of a prominence-to-corona transition region (PCTR) and a simulation that computes a hydrogen and helium system simultaneously.

The PCTR is the region where the hot corona and the cooler prominence interact, serving as an insulator for the prominence plasma from the corona, hence must be a key element to any simulation which hopes to have diagnostic potential. This issue was addressed by Labrosse and Gouttebroze in 2004 [18], following a study in 2002 of the PCTR and the signatures caused in hydrogen, helium and ionized calcium spectra [19]. Including the PCTR and having evaluated the resulting spectra, comparisons were drawn using two different solar prominence atmospheres: one which had isobaric and isothermal conditions, and the other which was non-isobaric and non-isothermal. It was found that the inclusion of a PCTR did have an effect on the D_3 (and other triplet) lines by altering their intensities. This was unexpected, as triplet lines are formed in the centre of the prominence. This suggested that a PCTR must be considered when predicting line emissions, regardless of the region in which they are formed. Other findings used level populations to show how statistical equilibrium changed with the inclusion of a PCTR, due to

it reducing the impact of collisional excitations with respect to populating energy levels. Again, this simulation noted a linear relationship between the D_3 line and the 10830 \AA line - a key result in agreement with the 2001 paper [17]. They also established that a correlation existed between the intensity ratios of these lines and the height of the slab above the solar surface, suggesting that one can predict the intensity of a triplet line if the intensity of the other line and the height was known. This paper settled the question around the inclusion of a PCCTR in any diagnostic solar prominence code and presented the first detailed analysis of the He I triplet lines.

In 2009, an alternative method was proposed by Léger and Paletou, in which they used 2D slabs to account for the criticisms discussed [21]. It was argued that neglecting fine structure caused the “unrealistic” Gaussian distributions that Labrosse and Gouttebroze achieved previously, and they also could not account for coronal illumination at the top of the slab or include any dilution effects which varied with altitude [17,18]. However, the Léger and Paletou model did not take into account the partial redistribution in frequency of resonance lines, whereas the Labrosse and Gouttebroze model introduced such an idea, whilst also using a more detailed helium model. A PCCTR is also absent from

this newly proposed model. Comparing their results to the work of Labrosse and Gouttebroze, the emergent intensities of D_3 and 10830 \AA follow the same pattern, but not in complete agreement. The reason for this was the partial redistribution function, or lack there-of. This proved that the D_3 emission is influenced by partial redistribution, which would be correct theoretically, as the lowest level of the D_3 emission is level four. Once again, and against the initial assertions of Léger and Paletou, the D_3 transition was found to be optically thin, which had previously been subject to debate [24]. This posed the question: what kind of model can produce results which show the D_3 emission to be optically thick under certain circumstances? Léger proposed the use of a 2D multi-thread model, however the intensity ratio ($D_3/10830 \text{ \AA}$) did not agree with observed data, with the exception of a high temperature high pressure scenario. For future work, they hypothesised that the inclusion of a PCCTR of every thread may provide the desired

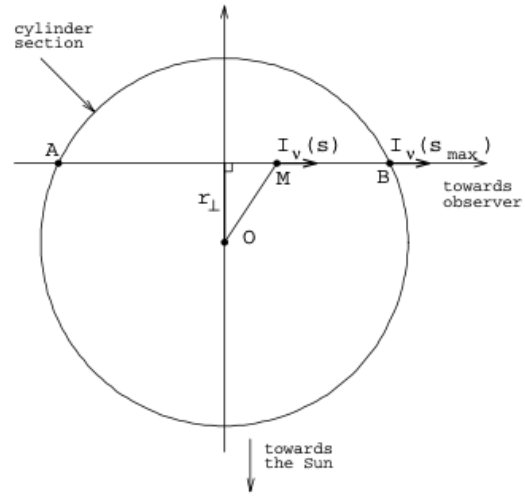


Figure 1.2: A graphic of the cylindrical approach used in Labrosse 2009, showing a ray of light passing through the cylinder. [14]

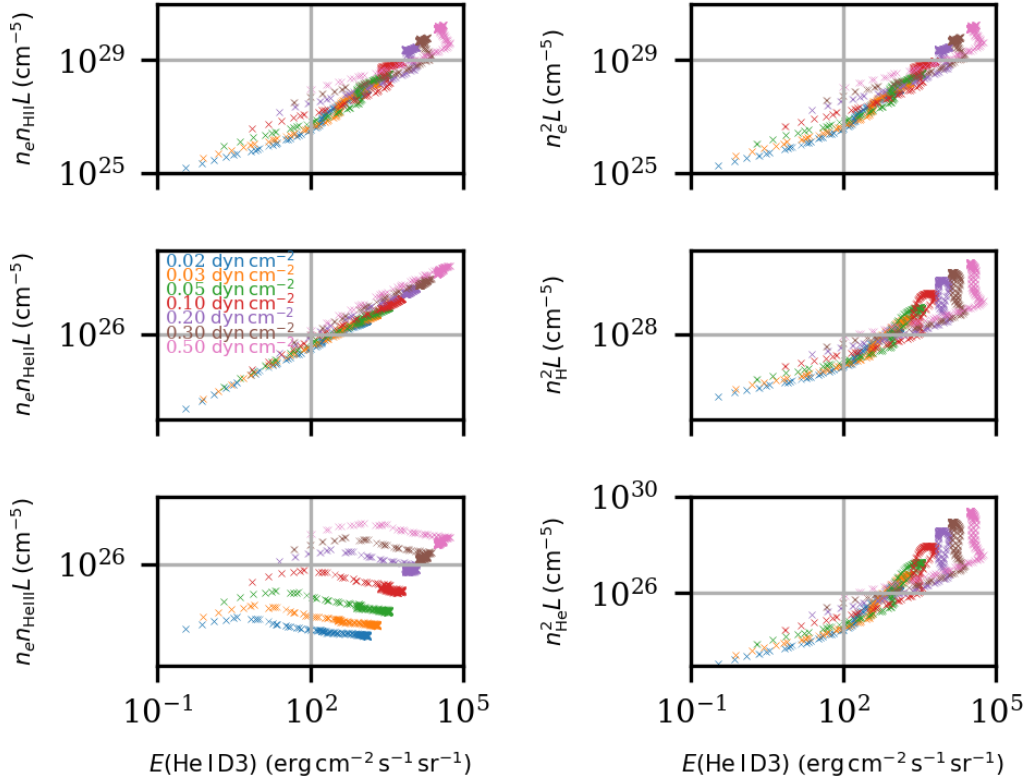


Figure 1.3: These plots show various forms of the emission measure against the integrated intensity of the D₃ emission. Adapted from reference [31].

outcome, but there have been no further publications to date.

Of all the issues and results discussed, each paper evaluated the different problems faced in trying to code an accurate radiative transfer simulation. Accumulating the findings and results of the previous papers led to a new code with potential for practical diagnostic applications. Published in 2009, the C2D2E code introduced a hydrogen and helium system using cylindrical geometry as opposed to plane-parallel slabs. This method provided a more realistic approach to prominences, as they are more cylindrical in nature [37]. The geometry of this approach is shown in figure 1.2. Again, this simulation found that the D₃ and 10830 Å lines were optically thin, in agreement with previous work. These lines also displayed the same temperature dependence, following the same pattern as each other, and displaying an increase in intensity between temperatures of 15,000 K and 30,000 K. The integrated intensity of both lines also increased linearly

with pressure. The authors acknowledge the need for the inclusion of motions in the helium routines and treating Lyman lines with partial frequency redistribution. However, this code was an important step forward due to it operating using 2D cylinders. This allowed for greater insight into how a line is formed and in what regions, through the use of techniques such as the contribution function. Due to the code dealing with both hydrogen and helium inside the cylindrical threads, this code presented the most up to date and accurate simulations of prominence events, with the authors currently working on adding additional elements such as carbon and magnesium.

With the use of the C2D2E code discussed previously, the level populations and electron densities were used to analyse various forms of the emission measure [31]. As shown in figure 1.3, the emission measures were plotted as a function of the integrated intensities of the D_3 transition. Model dependent emission measure increases were found in the majority of the plots, however the electron doubly helium plot (bottom left) showed no correlation between models. Interestingly, the electron singly ionized helium emission measure displayed a linear dependency, suggesting that a relationship exists between this emission measure and the integrated intensity of the D_3 emission. For example, if we could measure the length line of sight, the electron density, and the intensity of the D_3 transition, a direct measurement of the singly ionized helium density can be made. Additionally, contour maps provided information on the evolution of the contribution function throughout the cylinder. This showed how the pressure models and a millimetre-continuum at 3mm evolved, resulting in the conclusion that the D_3 emission remained optically thin, but the 3mm continuum became optically thick under higher gas pressures. In addition, the strong ring structure from the D_3 plots suggested that the line was formed in part in a specific region of the PCTR, going against the widely held assertion that the D_3 line is formed exclusively in the central regions of a prominence.

Proposed in 2015, the PROBA-3¹ mission consisted of the ASPIICS² coronagraph system in a constant solar orbit, becoming the first simultaneous flying system to provide continuous observational data of the solar atmosphere [30]. On this instrument's filter wheel, a D_3 filter will be used, posing the question of which narrow band filter would be most suitable? Using the 1D radiative transfer code developed by Labrosse and Gouttebroze in 2001 [17], a paper which proposed the narrow-band transmittance characteristics for the D_3 filter was published in 2018 [16]. This looked at the possibility of contamination from nearby sodium emissions using a D_3 filter, but also the viability of the filter being used to detect passing comets. Through computing various model variations, such as different temperatures or line-of-sight velocities,

¹PROBA - Project for On-Board Autonomy

²ASPIICS - Association of Spacecraft for Polarimetric and Imaging Investigation of the Corona of the Sun

this allowed for the conclusion of an optimal filter bandwidth of 20 Å. This is either flat or between flat and Gaussian, due to the lack of information surrounding the line-of-sight velocities.

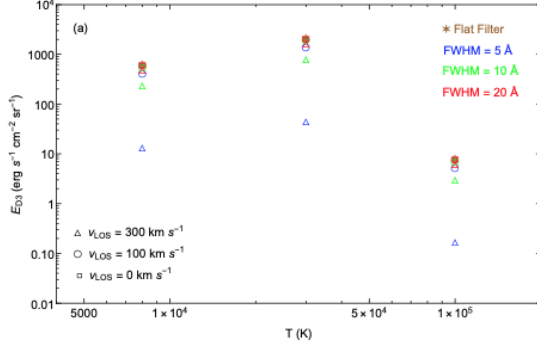


Figure 1.4: This figure shows the results from simulations plotting integrated intensity against temperature. Adapted from reference [16].

the cylindrical radiative transfer code developed by Labrosse and Gouttebroze in 2009 [14] and draw comparisons to the 1D results from the ASPIICS recommendations published in 2018 [16].

As well as the analysis conducted for ASPIICS, a similar exercise was conducted for METIS³ in 2020 [10]. This paper assessed the potential for detecting the D₃ emission alongside its linear polarization. To run the simulations, they used the 1D radiative transfer code developed by Labrosse and Gouttebroze in 2001 and 2004 to compute the electron densities for hydrogen and helium, before expanding these results into various other prominence parameters [17, 18]. Primarily, these 1D results showed that METIS will detect the D₃ emission alongside its linear polarization. Emission peaks at 30,000 K were found when

plotting integrated intensity of D₃ as a function of temperature, as shown in figure 1.5. This is theorised to be caused by ionization of the He I atom, causing it to become He II, and then this

Alongside this recommendation, they also recommended a flat 30 Å filter for comet detection, giving the device dual purpose and more economical. However, this filter may diminish the D₃ signal, and was estimated to be more vulnerable to contamination from prominence sodium lines. In addition, they found that peaks in D₃ intensity occur at 30,000 K for all models, as shown in figure 1.4. It is the goal of this research project to further explore the diagnostic potential of the D₃ line. Whilst the recommendations discussed used a 1D radiative transfer code [17], this project will use

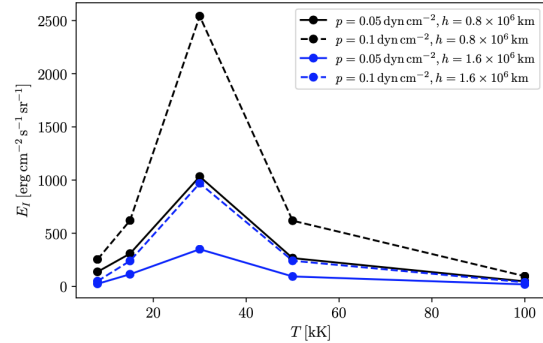


Figure 1.5: This figure shows the results from 1D simulations computing the integrated intensity of the D₃ emission plus visible light contributions against temperature. This figure was adapted from reference [10].

³Multi-Element Telescope for Imaging and Spectroscopy

He II recombines into the D_3 levels, causing the emission of photons. However, more research is required to analyse the population levels of He II at 30,000 K . The Q/I polarization ratio was found to be weak at 30,000 K , due to the observed intensity of the D_3 emission plus visible light. Whilst this was a disadvantage, the potential of using magnetic field diagnostics from other temperatures did produce promising results. Currently, it is the goal for researchers to assess all diagnostic capabilities from ASPIICS and METIS, with the goal of forming a synergy between the two coronagraphs. Hence, this project will also use the results from this paper in the analysis, with the aim of analysing and differences caused by the extra dimension. This will contribute towards forming a relationship between the capabilities of METIS and ASPIICS, which will benefit solar atmospheric research for the foreseeable future.

Chapter 2

Theory

2.1 The Basics of a Solar Prominence

Worshipped throughout centuries, the sun has been a source of constant fascination. From intense nuclear fusion at the core to the ejection of high energy particles from the Corona and presence of complex magnetic field structures, the sun's influence can be felt throughout the solar system. It is made up of seven main regions: the core; radiation zone; convection zone; photosphere; chromosphere; transition region; and the corona. The regions which a prominence directly influences (depending on what type of prominence it is) is the photosphere, chromosphere and the corona. The photosphere is the region of the sun in which sunspots form, showing where the magnetic field breaks through. Located just above, the chromosphere glows red during solar eclipses due to the burning of hydrogen, varying in temperature due to height. The corona appears as white streamers/plumes during solar eclipses, reaching temperatures of 2.5 MK , presenting one of the more well publicised problems in solar physics. The corona is an important region in solar atmosphere research, as it has a huge influence on the solar wind, which can have a direct influence on Earth.

The coronal heating problem is not of interest in this project, however the phenomenon under investigation may have a part to play in the eventual solution. In general, a solar prominence emerges from the photosphere, through the chromosphere and can extend into the corona. Due to the magnetic field structure, a prominence is similar in temperature and density to the chromosphere, with the plasma insulated against the intense coronal temperatures by the magnetic field, resulting in a PCTR. Typical values of density are between 10^{10} and 10^{11} cm^{-3} , and temperature is $\geq 10^4\text{ K}$, making it a factor of 10^2 cooler than the corona on average [20, 36].

There are three main regimes in which a prominence is classed: active region; quiescent; and intermediate. The difference between each is not governed by formation mechanisms, but by their scale and location in the solar atmosphere. An active region prominence is characterised by the low formation altitude and being located relatively close to sunspots in the photosphere. They have a higher probability of erupting, due to being in close proximity of active regions, giving them a timescale of merely hours. They vary in length between 5-30 Mm , and in width by 0.35-0.65 Mm [20,36]. In contrast, a quiescent prominence is a far larger structure extending well into the corona. These typically extend to a height of 50 Mm , a length between 10-100 Mm and a width between 1-10 Mm [20,36]. When the magnetic structure fails, the quiescent prominence becomes eruptive, as shown in figure 2.1. In between these regions exist intermediate prominences. They are identified as being a mix of active region and quiescent properties, depending on the section of the prominence under observation. They often occur near decaying active regions in the solar atmosphere.



Figure 2.1: An eruptive quiescent prominence observed by the Solar Dynamics Observatory on the 31st of August, 2012. [27]

2.2 Radiative Transfer Modelling

This section will detail the theory behind the radiative transfer modelling employed in the model used, starting from the basic derivation of the radiative transfer equation in section 2.2.1, and then detailing the statistical equilibrium in non-local thermodynamic equilibrium (NLTE) conditions in section 2.2.2.

2.2.1 Basic Radiative Transfer

By definition, radiative transfer describes the process of energy transfer via electromagnetic radiation. By solving the radiative transfer equations (RTE) under certain boundary conditions, one can deduce properties about the radiation field, such as the intensity of the emitted radiation, the level population, and so on. The basic form of the RTE describes the specific intensity $I(\nu)$ of the radiation along a path ds in a 1D prominence slab, similar to that shown in figure 1.1. This is given as

$$\frac{dI_\nu}{ds} = -k_\nu I_\nu + \eta_\nu \quad (2.1)$$

where the frequency of the radiation is given by ν , k is the absorption co-efficient and η is the emission co-efficient. Since this is in one-dimension, it holds that

$$\frac{dx}{ds} = \cos\theta \equiv \mu \quad (2.2)$$

where θ is the angle between the z axis and the spectral emission. In plane-parallel slab models, θ is set to zero, where θ is the angle between the incident radiation and the line of sight. Another important parameter is the optical depth τ , which characterises the conditions in which the emission lines are formed. This can be written as

$$d\tau_\nu = -k_\nu dx. \quad (2.3)$$

The RTE can now be expressed in a more complete form with the combination of these factors, giving

$$\mu \frac{dI_\nu}{d\tau_\nu} = I_{\nu,\mu} - S_\nu \quad (2.4)$$

where S_ν is the source function, defined as

$$S_\nu \equiv \frac{\eta_\nu}{k_\nu}. \quad (2.5)$$

Introducing the term y , representing the process which has been undergone, the total source function is

$$S_\nu^{TOT} = \frac{\sum_y \eta_\nu^y}{\sum_y k_\nu^y}. \quad (2.6)$$

The source function gives the ratio of emission to absorption in a medium. Examples of the processes represented by y would be bound-bound, free-free and bound-free transitions. Expanding the source function to include terms for the transitions from level i to level j , dependent on energy level populations, is

$$S_{\nu,y} = \frac{n_j A_{ji} \psi(\nu - \nu_0)}{n_i B_{ij} \phi(\nu - \nu_0) - n_j B_{ji} k(\nu - \nu_0)} \quad (2.7)$$

where ji and ij denotes emission and absorption respectively, A and B signify spontaneous and stimulated radiative processes respectively, and ψ, k^1 and ϕ^2 are the profiles for each process. From these equations, the mean intensity of the radiation field J_ν is derived as

$$J_\nu = \frac{1}{2} \int_{-1}^1 I_{\nu,\mu} d\mu. \quad (2.8)$$

Taking the radiative transfer in equation 2.4, multiplying it by an exponential factor e^{τ_ν} , and integrating over the optical thickness (due to optical thickness not being uniform throughout the medium) gives

$$I_\nu(L) = I_\nu(0) e^{-(\tau(L) - \tau(0))} + \int_{\tau_\nu(0)}^{\tau_\nu(L)} S_\nu(t_\nu) e^{-(\tau_\nu(L) - \tau_\nu)} dt_\nu. \quad (2.9)$$

In the wider literature, it is common to find calculations using wavelength λ in Å, as opposed to frequency in Hz. In order to use these principles in a more complex setting (such as a cylindrical thread 2D model), they must be adjusted and expanded to suit.

2.2.2 C2D2E Radiative Transfer & Statistical Equilibrium

C2D2E is the 2D cylindrical code utilised in this project. It solves the radiative transfer and statistical equilibrium equations for a hydrogen and helium system [14]. Retaining the frequency dependency used in the previous section, and expanding the radiative transfer equation for two

¹Induced/stimulated emission profile

²Extinction profile

dimensional simulations gives

$$\frac{dI(\Delta\nu, \mathbf{n})}{ds} = k_{ij}(\Delta\nu, \mathbf{n})[S_{ij} - I(\Delta\nu, \mathbf{n})]. \quad (2.10)$$

Here, \mathbf{n} is the direction of the ray, and $\Delta\nu$ is the difference in frequency with frequency line centre at ν_{ij} . The term k_{ij} is the absorption coefficient for a spectral line, given as

$$k_{ij}(\Delta\nu, \mathbf{n}) = k_{ij}^M \phi(\Delta\nu, \mathbf{n}) \quad (2.11)$$

where

$$k_{ij}^M = \frac{h\nu_{ij}}{4\pi} (n_i B_{ij} - n_j B_{ji}). \quad (2.12)$$

In equation 2.10, the source function has been simplified from the version in equation 2.7, due to the assumption of complete frequency redistribution, giving

$$S_{ij} = \frac{n_j A_{ji}}{n_i B_{ij} - n_j B_{ji}}. \quad (2.13)$$

Using solid angle Ω , and structuring the equation such that it is solved in terms of frequency and direction, the mean intensity \bar{J}_{ij} is

$$\bar{J}_{ij} = \frac{1}{4\pi} \int_{-\infty}^{+\infty} d(\Delta\nu) \oint I(\Delta\nu, \mathbf{n}) \phi(\Delta\nu, \mathbf{n}) d\Omega \quad (2.14)$$

where

$$\phi(\Delta\nu, \mathbf{n}) = \frac{1}{\sqrt{\pi} \Delta\nu_D} H\left[a, \frac{1}{\Delta\nu_D} \Delta\nu\right] \quad (2.15)$$

is the normalised profile. In this, a is a damping factor which takes in to account various forms of line broadening mechanisms, H is the Voigt function, and $\Delta\nu_D$ is the Doppler width of the emission profile.

Local Thermodynamic Equilibrium (LTE) is defined as a plasma which is the same temperature throughout, with a large collisional frequency but low photon losses. In LTE, the level populations can be found via the Saha-Boltzmann equations, which gives a Maxwellian distribution. A notable feature of LTE modelling is the balance between various processes, as they occur at the same rate. For example, emission would occur at the same rate as absorption. This is a suitable approximation for the solar interior, and also holds up for events in the lower photosphere. For prominence structures, an LTE would not be suitable.

For this research, a non-Local Thermodynamic Equilibrium (NLTE) approximation is more appropriate, due to the prominence structures being analysed being quiescent. NLTE is characterised by a plasma which has a large photon loss and a large amount of scattering. Expanding on these ideas, non-local radiation transport is considered due to external radiation incident upon the prominence. Statistical equilibrium refers to time-dependent level populations, with the equations of statistical equilibrium solved to calculate the level populations in NLTE modelling. The statistical equilibrium equation, at time equal to zero, is given as

$$\frac{dn_i(\vec{r})}{dt} = \sum_{j \neq i}^n n_j(\vec{r})P_{ji}(\vec{r}) - n_i(\vec{r}) \sum_{j \neq i}^n P_{ij}(\vec{r}) = 0 \quad (2.16)$$

where N represents the number of levels that can influence the populations of a level n_i , and P_{ij} is given by

$$P_{ij} = A_{ij} + B_{ij}\bar{J}_{ij} + C_{ij} = R_{ij} + C_{ij} \quad (2.17)$$

where A_{ij} , B_{ij} and C_{ij} are the Einstein coefficients. For spontaneous emission, $A_{ij} = 0$. References [32, 33] were used extensively for this section and have more in depth reading about the Einstein coefficients. For C2D2E, and considering processes which depopulate level j into balanced levels i , such that

$$n_j \sum_{j \neq i}^n P_{ji} = \sum_{j \neq i}^n n_i P_{ij}. \quad (2.18)$$

In the above equation, the left-hand side represents all depopulation processes for level j , meanwhile the right-hand side represents the population processes for level j . The depopulation rate, like the population rate, can be stated as

$$P_{ji} = A_{ji} + B_{ji}\bar{J}_{ij} + C_{ji} = R_{ji} + C_{ji}. \quad (2.19)$$

To ensure there are no non-physical population levels,

$$\sum_{j=1}^j n_j = n_T \quad (2.20)$$

with n_T representing the total population of the atomic element being simulated.

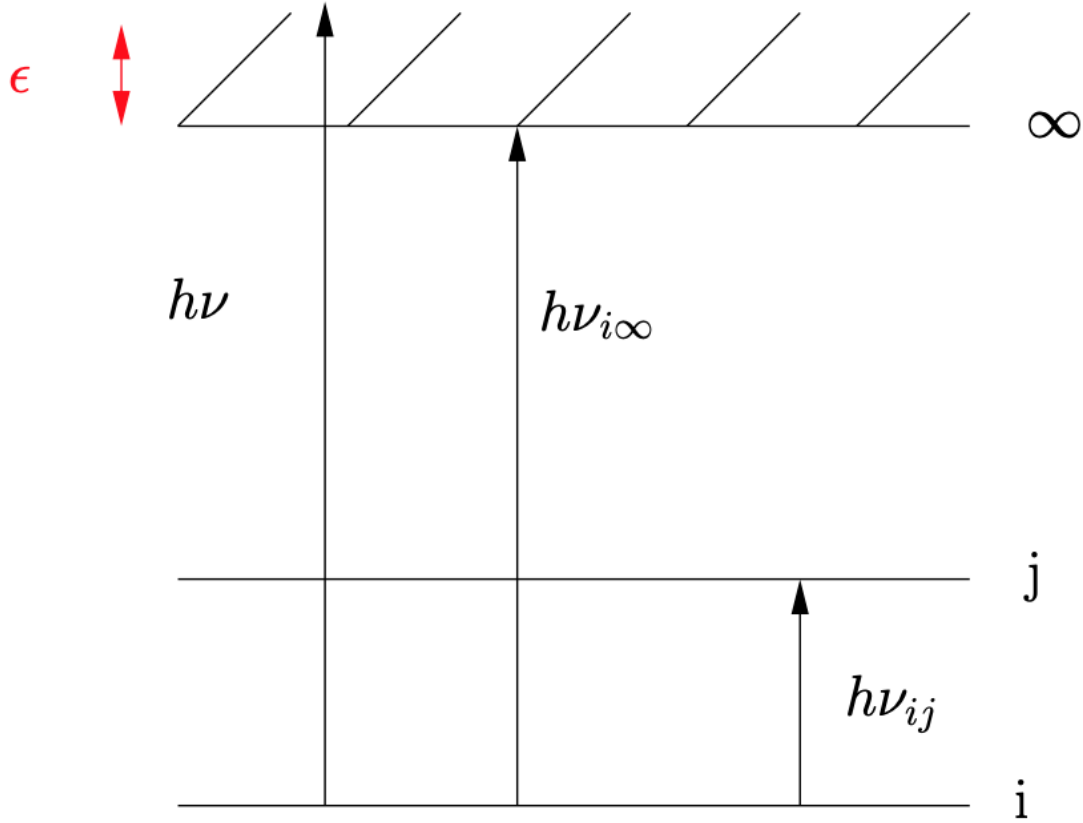


Figure 2.2: A transition diagram for the C2D2E code, showing bb and bf transitions. Adapted from reference [7].

2.2.3 Spectral Line Formation Mechanisms

In radiative transfer, there are three main solar radiation interactions which govern emissions: scattering, collisional, or a mix of both. In terms of the C2D2E code, it only includes mechanisms which allow both scatterings and collisions, namely bound-bound and bound-free interactions. The bound-free interactions (bf) feed the continua in the simulation, as an electron transitions from a bound state i into the solar continuum with energy ϵ , producing a photon. Bound-bound interactions (bb) take place between two bound levels, such as going from level i to j , and are particularly important as it can provide diagnostic information about the physical conditions of their formation region. A transition diagram for bb and bf transitions is shown in figure 2.2. Both bb and bf transitions can occur in many different pair combinations which describe the mechanisms of the transition (such as collisional excitation up, collisional de-excitation down) which can all occur within the code. Such mechanisms can be found in reference [32] in detail.

2.3 Wider Applications

Whilst radiative transfer modelling of a solar prominence is important to explore, it is also important to demonstrate the potential impact a reliable model will have on the wider research being conducted. Section 2.3.1 details the applicability of modelling in space-based coronagraphs, meanwhile section 2.3.2 discusses research conducted into prominence magnetic structure. In the long term, it is the goal that these research areas are bridged, as both have wide ranging applicability in the field of space weather.

2.3.1 Space Instruments

At the “Nature of Prominences and their role in Space Weather” conference in 2013, a review was conducted which evaluated the applications of ground-based telescopes against their space-based counterparts [23]. It was well known that ground-based telescopes are continually hampered in the field of prominence observations due to atmospheric effects. Whilst ground-based telescopes have their advantages, such as spectropolarimetry [24], space-based telescopes have the upper hand in any comparison. This is due to spatial resolution, fulfilling the signal-to-noise requirements, and the field of view in general [23], however currently this now varies by detector. In addition, space-based telescopes have access to wavelengths not accessible on Earth, due to atmospheric extinction, and continuous observations are not affected by daylight variations. Hence, with the growing accessibility of space, space-based telescopes can provide a wealth of information about a solar prominence that ground-based telescopes cannot match. It is with this in mind that substantial research must be carried out, to ensure the promise of space-based telescopes is not wasted.

On the 9th of February 2020, Solar Orbiter, a joint mission between the European Space Agency (ESA) and the National Aeronautics & Space Administration (NASA), was launched. The goal is to understand how the Sun controls the ‘bubble’ of plasma which surrounds the solar system, amongst other issues surrounding the solar wind. To achieve this, the craft would orbit up to within 0.3 AU of the Sun [2]. On board, METIS will present new opportunities for the scientific advancement of coronal studies [3]. To do this, it will primarily look to observe eruptive prominence structures and coronal mass ejections (CMEs). Observing simultaneously in visible and ultraviolet to perform imaging of the off-the-limb solar corona, the measurements performed

enable instant calculations of plasma properties such as the temperature, density and outflow velocities [10]. As of writing, initial observations from METIS have not been published, and are due sometime in late 2021. However, METIS has paved the way for space-based coronagraphs for future missions.

Projected to launch in mid-2022, the ESAs PROBA-3 mission boasts of being the world's first precision formation flying mission [1], carrying the ASPIICS coronagraph. This coronagraph operates using the two satellites, with the coronagraph satellite (CSC) housing the detector and the occulter satellite (OSC) carrying the Sun occulter disk. When flying in formation, the OSC blocks out between 1.08 and 3 solar radii (R_{sun}), allowing the CSC to gather data within the sonic point³ of the Sun [30]. The data that can potentially be gathered about the sonic point is not usually available, due to the brightness of the sun itself, meaning that the only opportunities for data collection so far came during a solar eclipse. PROBA-3 provides the opportunity for constant observations in this region of the sun, thus presenting a solution to the issue of sparse prominence data alongside METIS [15]. Simulations evaluating the optimal setup for ASPIICS established that a flat filter or a 20 Å filter would be best suited for the detection of the D₃ line, whilst reducing any risk of contamination from relatively close sodium lines [16]. However, D₃ may only be detectable in prominence events, and not in the surrounding corona. A 1 MK D₃ emissions emissivity would be at least one order of magnitude weaker compared to the nearby Iron Fe XII emissions, making it far more difficult for ASPIICS to detect clearly [8]. These findings highlight the importance of using ASPIICS in the correct circumstances to maximise results, and hint at the future diagnostic potential from the data it returns.

2.3.2 Magnetic Field Inference

Diagnostic potential is a clear end-goal for any potential radiative transfer prominence model. But alongside this, the role of physical observations and magnetic structure simulations cannot be understated. The D₃ transition holds vital information about the magnetic field which governs the prominence, acting as an insulator against the vastly hotter coronal plasma, and also supporting the shape of the prominence [9]. Hence, the interpretation of observational data works alongside theoretical predictions to yield a greater understanding about the mechanisms which dictate these prominence structures.

The possibility of obtaining information from prominence spectra was initially proposed in

³2-3 solar radii from the solar centre

1981. It was suggested that simultaneous polarization measurements at two different wavelengths can yield information about the magnetic field strength using the Hanle effect [5]. This became known as spectropolarimetry, with the THEMIS⁴ observatory in Tenerife conducting measurements which utilises the D₃ line [34]. Conversely, it is also possible to measure two different components of the D₃ transition. Analysing the atomic transitions $3d^3D_{3,2,1} \rightarrow 2p^3P_{1,2}$ and $3d^3D_1 \rightarrow 2p^3P_0$ can also give information about the magnetic field strength, however the spectral resolution must be precise, since these two components are separated by 34 pm [28]. Due to this, the spectropolarimetry approach led by THEMIS is primarily used in the area of observational prominence magnetic fields.

In 2002, to build on the spectropolarimetry approach, pattern recognition was used alongside principle component analysis (PCA) to quickly evaluate the wealth of data gathered by THEMIS [24]. This involves inverting the spectropolarimetric data from the D₃ line and using PCA on all four Stokes terms. Focusing on the D₃ line, it was suggested that relaxing the optically thin constraint in order to produce a reliable model, however a simple model was developed to calculate the Stokes profiles for the D₃ line which reproduced the main observational features required. This simple model included the optically thin limit but did not include any radiative transfer effects - something which influences the accuracy of their results. In previous simulations, the Stokes V term was neglected. However, including this term produced magnetic fields which exceeded 50 G. Previously, it was assumed that the magnetic fields within a solar prominence had strength 10-20 G. Thus, it was concluded that including all four Stokes terms (I, Q, U and V) is required when deducing the magnetic field strengths for accurate and insightful results.

Expanding on the PCA approach, the algorithm was applied in 2003 to data from a solar event on the fifth of August 1980 [25]. This event was originally analysed in 1985, with the data showing anomalies such that the optically thin D₃ line was shown to be optically thick [29]. However, it must be noted that this data was gathered forty years ago, and computing power has advanced significantly since. The 2003 analysis of the data could not provide an explanation for the optically thick D₃ line; however they did note an increase in the magnetic field strength of the prominence three hours before it erupted. This poses the question - is this a common theme which signals an erupting prominence? It was concluded that more data was required to verify this claim, but again this model does not bring into account radiative transfer effects. With the inclusion of radiative transfer modelling, behaviour of the intensity and polarisation profiles can be accounted for. However, more recent data was available. A Prominence which occurred in

⁴T  lescope H  liographique pour l'Etude du Magnetisme et des Instabilit   Solaires

2002 had been captured by the Dunn Space Telescope and provided the perfect opportunity to test the new algorithms on fresh data [6]. The analysis agreed with the previous papers discussed - the average magnetic field was between 10-20 G , field strengths of 50 G and above were possible due to the inclusion of the Stokes V term, and that (again) radiative transfer must be considered. Yet, the optically thin assumption was brought into question. It was found that the observed intensity ratios of the two visible components of D_3 did not match up with theoretical predictions. This may suggest a varying optical thickness of the D_3 line at different points in the prominence.

In the present day, spectropolarimetry is the standard procedure for magnetic field measurements in prominences. However, instances where this is possible are rare, hence reliable models which reproduce the magnetic field behaviour should be considered, alongside detailed analysis from space-based coronagraphs. A study of this possibility was conducted in 2020 [26]. In this, spectropolarimetric data from an event captured by THEMIS in 2013 was used to compare the results produced by two non-linear force free field models. These models were constructed as flux ropes, with one being strongly twisted and the other weakly twisted. The original THEMIS data using the D_3 line showed a variance in the magnetic field strength in the prominence, with one region displaying variations between 8-11 G , whilst other regions displayed variations between 11-18 G , indicating that the prominence has two distinct regions [35]. Constructing the models, it was found that a strongly twisted flux rope best replicated the results from THEMIS, showing that a flux rope best represents the magnetic field configuration in a prominence. This initial finding allows further research into magnetic flux rope modelling, and constructed alongside the radiative transfer codes developed previously, these can form a more accurate picture of the solar atmosphere than drawn previously.

Chapter 3

Methodology

3.1 C2D2E Routines & Calculations

In order to compute the prominence simulation, the C2D2E radiative transfer code is used [14]. To create the system of hydrogen and helium, two schemes are conducted simultaneously, one for each element. This simulation uses the level populations alongside geometric and physical variables to calculate the ionization, whilst storing the atomic structure variables (such as populations, transition intensities and atomic parameters) in a FORTRAN “common”. The procedure for the simulations is as follows:

1. The initialization stage calculates the parameters not stored in the common i.e. the level populations, geometric, and physical variables.
2. The level populations for each element is calculated using the optically thin approximation.
3. This computation uses incident radiation from outside of the prominence (like radiation coming from lower in the solar atmosphere). This incident radiation is averaged in order to calculate the mean intensities from the various helium/hydrogen transitions. This allows the radiative and collisional transition rates to be calculated.
4. At this point, solving the statistical equilibrium equations in an (r, ϕ) mesh allows the level populations for each point to be calculated.
5. From this, the transition rates are calculated. This was an iterative process, utilising the electron density.
6. Due to steps 4 and 5, the overall populations for each element (N_{HII} , N_{HeII} & N_{HeIII}) are deduced. Steps 2-6 are repeated until convergence.

This formed the initial stage of the calculations. After convergence and thus completion of this first stage, radiative transfer effects were then introduced.

1. The steps discussed previously are completed again, but on this occasion NLTE radiative transfer conditions is used.
2. The atomic level populations are used to derive the absorption coefficient.
3. As opposed to the previous step 3, the intensities of the transitions were calculated using the radiative transfer equation, solved in the direction of the ray path and integrated with respect to direction and frequency.
4. From the intensity calculations, a new statistical equilibrium equation is formed, which is then used to calculate the level populations.

3.2 The Models Used

The C2D2E code requires a number of different input parameters in order to run the simulations. Each set of parameters is defined as a model. For models which include a PCTR at an altitude of 10,000 *km*, we initially explore the effect that altering the helium abundance ratio has on the results. The helium abundance ratio in C2D2E is defined as the ratio of helium to hydrogen atoms within the cylinder. In these models, the radius of the cylinder is set to 1000 *km*, with the PCTR becoming active from a radius of 500 *km*, the central temperature is set to 8000 *K*, and the PCTR restricted to a maximum temperature of 100,000 *K*. The gas pressure is held constant in these models at 0.1 *dyn cm^{-2}* . To explore any effect, the helium abundance ratio varies between 0.050 to 0.300. These models are marked as "AB" in table 3.1. Notably, model AB2 has a helium abundance ratio of 0.085 calculated from observational data, detailed in reference [4]. Similarly, the models which vary the radius of the cylinder is shown in table 3.1, marked with an "R". These models keep the helium abundance ratio constant at 0.1, the gas pressure remains at 0.1 *dyn cm^{-2}* , the central temperature remains fixed at 8000 *K*, and the PCTR can reach a maximum temperature of 100,000 *K*. The radius of the cylinder is varied from 100 *km* to 5000 *km*, with the PCTR becoming active at 25% of the total radius. These PCTR models will be used to analyse various forms of the emission measure as a function of the integrated intensity of the D₃ emission, and the contribution function of certain models, in order to assess if any diagnostic information exists in these relationships.

The models which do not include a PCTR are shown in tables 3.2, 3.3 and 3.4. Primarily, these models have three parameters which vary between models, with the altitude changing be-

Model	Ab_{He}	R_0 (km)	R_1 (km)	Altitude (km)	T_0 (K)	T_1 (K)
AB1	0.050	500	1000	10000	8000	100000
AB2	0.085	500	1000	10000	8000	100000
AB3	0.100	500	1000	10000	8000	100000
AB4	0.150	500	1000	10000	8000	100000
AB5	0.200	500	1000	10000	8000	100000
AB6	0.250	500	1000	10000	8000	100000
AB7	0.300	500	1000	10000	8000	100000
R1	0.1	25	100	10000	8000	100000
R2	0.1	50	200	10000	8000	100000
R3	0.1	100	400	10000	8000	100000
R4	0.1	250	1000	10000	8000	100000
R5	0.1	500	2000	10000	8000	100000
R6	0.1	1250	5000	10000	8000	100000

Table 3.1: The parameters used for each model. Ab_{He} is the helium abundance for each model, R_0 is the radius from the centre of the prominence at which the PCTR begins, R_1 is the total radius, T_0 is the temperature inside R_0 , and T_1 is the maximum temperature inside the PCTR.

tween 800,000 km and 1,600,000 km, the temperature changing from 8000 K to 100,000 K, and the model variable such as helium abundance ratio, gas pressure, or the radius of the cylinder. For models which look at the effect of the helium abundance ratio, values of 0.085 and 0.300 for the abundance ratio are used, with gas pressure held constant at 0.1 dyn cm^{-2} and radius held constant at 2500 km. These models are shown in table 3.2. For models which look at the effect of gas pressure, values of 0.05 and 0.1 dyn cm^{-2} for the gas pressure are used, which replicates the models used in references [10, 16]. For these models, the helium abundance ratio is constant at 0.1, and the radius of the cylinder is constant at 2500 km. These models are summarised in table 3.3. For models which look at the effects caused by changing the cylindrical radius, values of 1000 km and 2500 km for the cylindrical radius are used, with the helium abundance ratio constant at 0.1 and the gas pressure constant at 0.1 dyn cm^{-2} . These models are summarised in table 3.4.

From these processes and models, the data was analysed using python code developed by Dr. Andrew Rodger [31]. This combines the results produced by the 2D cylindrical radiative transfer code used in 2009 [14], based on the cylindrical mathematics for prominences from 2005 [11]. For models marked with a “*” in tables 3.2, 3.3 and 3.4, these models displayed non-physical results in the latter stages of the final calculations by showing a negative optical thickness. This

Model	Pressure (dyn cm^{-2})	Ab_{He}	Radius (km)	Altitude (km)	Temperature (K)
AB01*	0.1	0.085	2500	800000	8000
AB02	0.1	0.085	2500	800000	15000
AB03	0.1	0.085	2500	800000	30000
AB04	0.1	0.085	2500	800000	50000
AB05	0.1	0.085	2500	800000	100000
AB06	0.1	0.085	2500	1600000	8000
AB07	0.1	0.085	2500	1600000	15000
AB08	0.1	0.085	2500	1600000	30000
AB09	0.1	0.085	2500	1600000	50000
AB10	0.1	0.085	2500	1600000	100000
AB11*	0.1	0.300	2500	800000	8000
AB12	0.1	0.300	2500	800000	15000
AB13	0.1	0.300	2500	800000	30000
AB14	0.1	0.300	2500	800000	50000
AB15	0.1	0.300	2500	800000	100000
AB16*	0.1	0.300	2500	1600000	8000
AB17	0.1	0.300	2500	1600000	15000
AB18	0.1	0.300	2500	1600000	30000
AB19	0.1	0.300	2500	1600000	50000
AB20	0.1	0.300	2500	1600000	100000

Table 3.2: Models which altered the helium abundance ratio with no PCTR present. “*” highlights the models which displayed non-physical properties.

is briefly discussed in the results section.

Model	Pressure (dyn cm^{-2})	Ab_{He}	Radius (km)	Altitude (km)	Temperature (K)
P01	0.05	0.1	2500	800000	8000
P02	0.05	0.1	2500	800000	15000
P03	0.05	0.1	2500	800000	30000
P04	0.05	0.1	2500	800000	50000
P05	0.05	0.1	2500	800000	100000
P06*	0.05	0.1	2500	1600000	8000
P07	0.05	0.1	2500	1600000	15000
P08	0.05	0.1	2500	1600000	30000
P09	0.05	0.1	2500	1600000	50000
P10	0.05	0.1	2500	1600000	100000
P11	0.1	0.1	2500	800000	8000
P12	0.1	0.1	2500	800000	15000
P13	0.1	0.1	2500	800000	30000
P14	0.1	0.1	2500	800000	50000
P15	0.1	0.1	2500	800000	100000
P16*	0.1	0.1	2500	1600000	8000
P17	0.1	0.1	2500	1600000	15000
P18	0.1	0.1	2500	1600000	30000
P19	0.1	0.1	2500	1600000	50000
P20	0.1	0.1	2500	1600000	100000

Table 3.3: Models which altered the gas pressure with no PCTR present. “*” highlights the models which displayed non-physical properties.

Model	Pressure (dyn cm^{-2})	Ab_{He}	Radius (km)	Altitude (km)	Temperature (K)
RAD01*	0.1	0.1	1000	800000	8000
RAD02	0.1	0.1	1000	800000	15000
RAD03	0.1	0.1	1000	800000	30000
RAD04	0.1	0.1	1000	800000	50000
RAD05	0.1	0.1	1000	800000	100000
RAD06*	0.1	0.1	1000	1600000	8000
RAD07	0.1	0.1	1000	1600000	15000
RAD08	0.1	0.1	1000	1600000	30000
RAD09	0.1	0.1	1000	1600000	50000
RAD10	0.1	0.1	1000	1600000	100000
RAD11	0.1	0.1	2500	800000	8000
RAD12	0.1	0.1	2500	800000	15000
RAD13	0.1	0.1	2500	800000	30000
RAD14	0.1	0.1	2500	800000	50000
RAD15	0.1	0.1	2500	800000	100000
RAD16*	0.1	0.1	2500	1600000	8000
RAD17	0.1	0.1	2500	1600000	15000
RAD18	0.1	0.1	2500	1600000	30000
RAD19	0.1	0.1	2500	1600000	50000
RAD20	0.1	0.1	2500	1600000	100000

Table 3.4: The models altering the cylindrical radius with no PCTR present. “*” highlights the models which displayed non-physical properties.

Chapter 4

Results

The results are split up as such: section 4.1 analyses different forms of the emission measure as a function of D_3 intensity and the corresponding contribution function of the emission by altering the abundance ratio of helium present in the simulations; section 4.2 provides the same analysis but for models in which the radius of the cylinder has been altered; and section 4.3 uses isobaric-isothermal models to compare the average intensity of the D_3 emission against the temperature of the model. For reference, sections 4.1 and 4.2 are being compared to the work completed by Dr. Andrew Rodger [31], and section 4.3 will compare the results against these references [10, 16]. The tables detailing the parameters for each model can be found in section 6.2 in the appendix.

4.1 Altering the Helium Abundance Ratio

Since the helium abundance ratio can vary between different prominences, it was decided to alter this parameter to see how this had an effect on the results. The abundance value of 0.085 (rounded up to 0.09 in the graph legends) was taken from a previous paper detailing physical calculations [4]. The details of each model can be found in table 3.1. Figure 4.1 shows different forms of the emission measure as a function of the integrated intensity of the D_3 emission. Altering the helium abundance ratio has pushed the model dependent increases in emission measure closer together when compared to the gas pressure variant models from reference [31] and shown in figure 1.3, where the increases in emission measure across the different models were notably separated. This is also the case for the electron-doubly-ionized helium emission measure plot (bottom left), although this plot shows little diagnostic potential due to a lack of any clear relationship. The electron-singly-ionized helium emission measure in the left middle plot continues

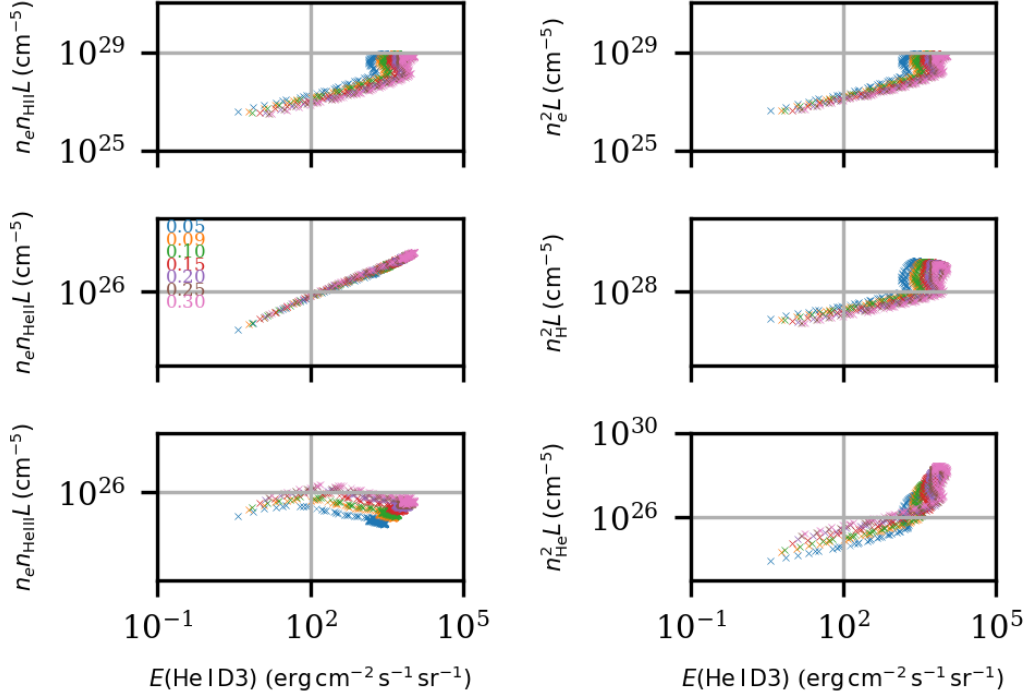


Figure 4.1: This figure shows various forms of the emission measure as a function of the integrated intensity of the D₃ transition for models which alter the helium abundance ratio. Note, the 0.09 abundance is model AB2, with an abundance ratio of 0.085.

to show a clear linear dependency between emission measure and intensity, implying that there are diagnostic applications for this relationship. For example, if one could measure the length of the line of sight, the D₃ intensity and the electron density, we can calculate the intensity of singly-ionized helium. Beforehand, this plot did display hint at model dependent emission measure variations for the pressure variant models whilst remaining linear. However, keeping gas pressure constant has improved the linearity of this plot, which suggests that the gas pressure does have an impact on the model dependent increases.

The contribution functions for selected abundance ratio models is shown in figure 4.2. This plot shows what areas of the cylinder makes the most contribution with regards to the formation of the D₃ emission. At an abundance ratio of 0.05, the emission is optically thin as the plot is symmetric. The majority of the contribution comes from the centre of the cylinder, which is slightly biased towards the bottom of the cylinder, and the ring structure shows that some line formation does take place in the PCTR. This ring structure can clearly be seen across all



Figure 4.2: This figure shows how the D_3 line emission evolves using the contribution function and the data produced by models AB1, AB4 and AB7 from table 3.1. The contour levels correspond to 20, 40, 60, 80 100% of the contribution function in the prominence.

abundance ratio contribution plots. For reference, in figure 6.1, the contribution functions for D_3 and He I 584 Å are shown. This shows the formation region of the 584 Å line, which is an optically thick emission where the line formation occurs within the PCTR. This gives an idea of where the PCTR is located in comparison to the D_3 emission. At an abundance of 0.15, the contribution begins to become biased towards the bottom of the cylinder, and this trend continues with an abundance of 0.30. This is caused by the incident radiation from the solar disk hitting the bottom of the cylinder, with the incident radiation causing more scattering of helium atoms and hence more emissions. In addition, altering the helium abundance ratio causes the statistical equilibrium solutions to change and thus the electron density changes between models. This may cause a greater level population for neutral helium, which may result in helium I becoming ionized to helium II, and then helium II recombines into the upper levels of the D_3 emission. This process will cause a transition between the upper and lower levels of the D_3 transition, resulting in the emission of D_3 photons. However, more research is required to fully investigate and prove this effect. Again, the strong ring structure remains across all three models, and when comparing to figure 6.1, this shows that any contribution coming from the PCTR is coming from the interior of the PCTR and not near the edge of the cylinder. This does pose the question of where the D_3 line is formed, since it is generally accepted to be formed at the centre of the prominence.

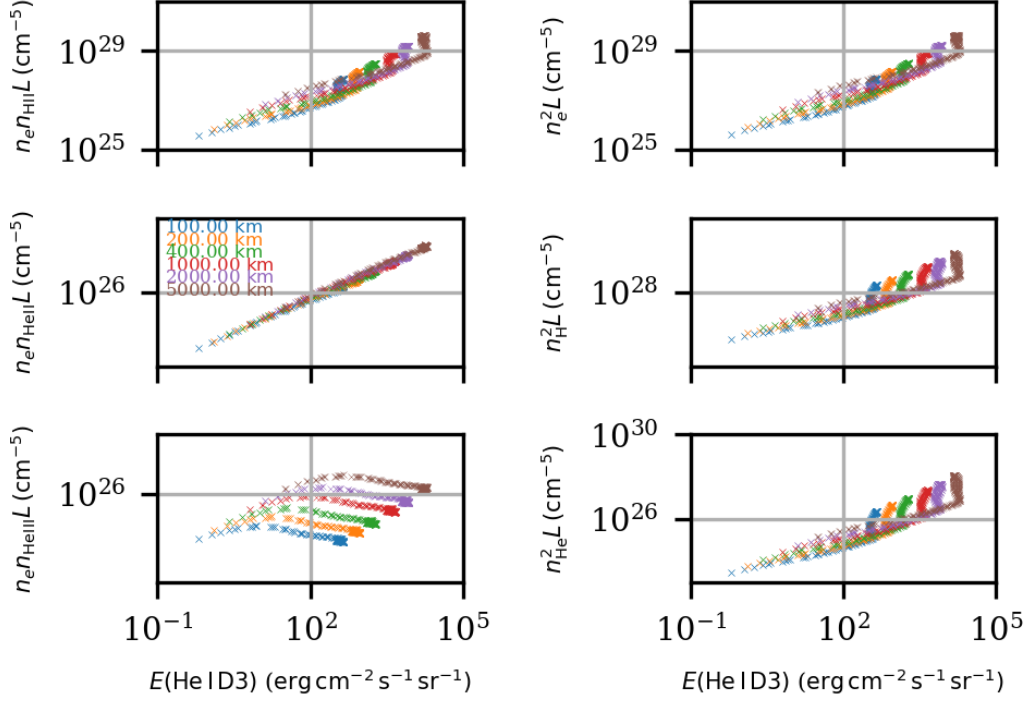


Figure 4.3: This figure shows the various forms of the emission measure as a function of the integrated intensity of the D₃ emission produced by models R1, R4 and R5 from table 3.1.

4.2 Altering the Cylindrical Radius

Since the size of a prominence can vary from event to event, it is important to run simulations which explore how the results change by altering the cylindrical radius. Again, figure 4.3 shows different forms of the emission measure plotted as a function of the integrated intensity of D₃. The electron-singly-ionized helium emission measure (left middle) continues to display a linear relationship similar to that seen in figure 4.1. However, the model dependent emission measure increases seen in figure 4.1 are not reproduced, instead these models have model dependent peaks in emission measure across a range of integrated intensities. This is caused by the changing length (L) in the emission measure, due to the various radius values and thus altering the length of the line-of-sight between each model. Again, in comparison to the gas pressure dependent models shown in figure 1.3, it can be seen that gas pressure is the prime contributing factor governing the model dependent emission measure increases seen across the vast majority of the emission measures.



Figure 4.4: This figure shows how the D_3 line evolves using the contribution function and the data produced by the models altering the cylindrical radius, using values of 100 km , 1000 km and 2000 km . The contour levels correspond to 20, 40, 60, 80 100% of the contribution function in the prominence.

The contribution functions for three models which change the cylindrical radius are shown in figure 4.4. Similar to the models dependent on the helium abundance ratio, there is a strong ring structure displayed across all three models. This indicates a significant amount of D_3 line formation takes place in the PCTR (see figure 6.2 in the appendix for a comparison against the 584 Å line). In the radius of 100 km plot, this shows a completely symmetric distribution across the cylinder, showing that the plasma is optically thin at all points. There are similar contributions from the centre of the cylinder and in the PCTR, showing that the line formation regions are split. This is due in part to the size of the prominence itself, since a cylindrical radius of 100 km is a relatively small structure in the solar atmosphere. For the 1000 km plot, the contribution from the PCTR has reduced, as shown by the less-prominent ring structure when compared to the other two plots. Much of the D_3 line formation occurs at the centre of the cylinder, with the contribution slightly biased towards the bottom of the cylinder due to the incident radiation from coronal illumination. The same can be seen in the 2000 km plot. What is interesting about the 2000 km plot is the re-emergence of the strong ring structure as seen in the 100 km plot, with the difference being that the PCTR contributes more than the centre of the prominence. This is an indicator that, in larger prominence structures, there is a possibility that much of the formation of the D_3 originates from the PCTR and less-so from the more central regions.

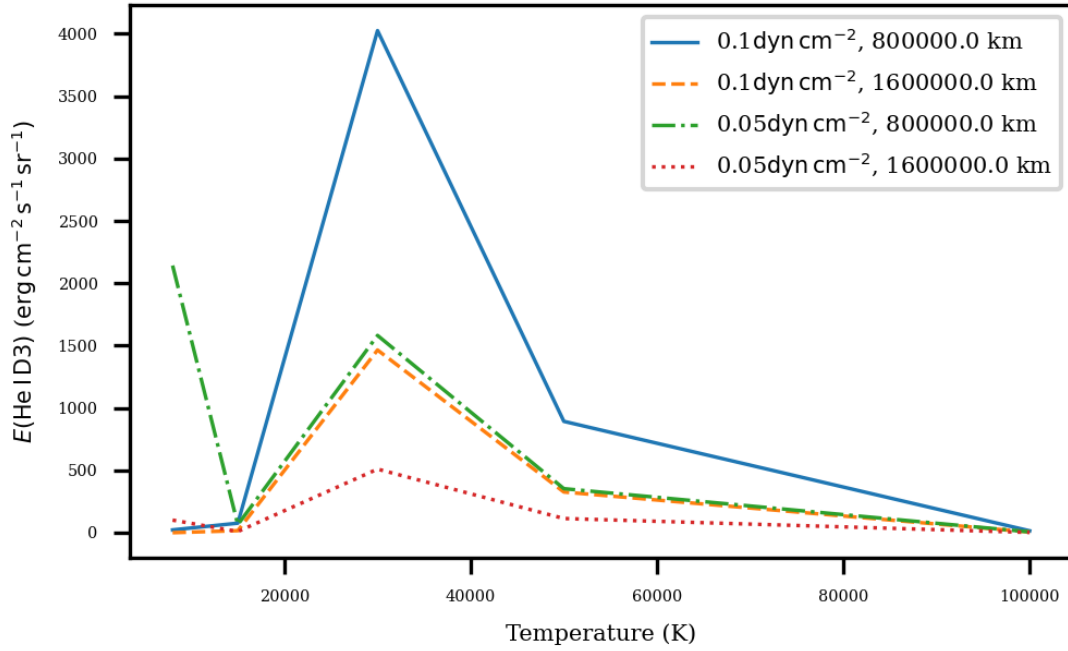


Figure 4.5: This figure shows the results from models altering the gas pressure, showing integrated intensity of the D₃ emission as a function of the temperature. The graph legend displays the gas pressure and the altitude of each model.

4.3 Integrated Intensity of the D₃ Emission as a Function of Temperature

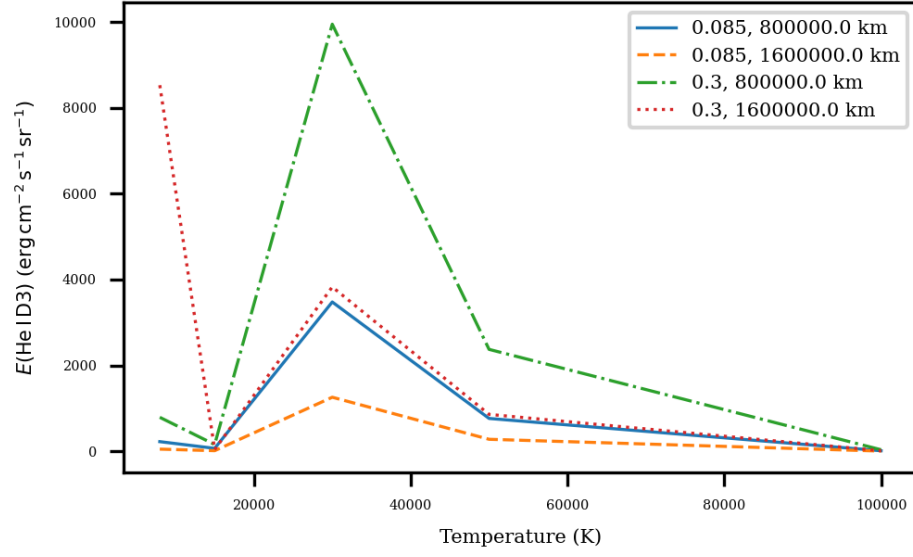
To complete this analysis, models were simulated which altered the gas pressure, helium abundance ratio and radius of the cylinder. The details of each model can be found within tables 3.2, 3.3 and 3.4. These models did not include a PCSTR, thus keeping gas pressure and temperature constant throughout the cylinder. One issue that arose with a minority of the models at 8000 *K* (models marked with a “*”) as they displayed a negative optical thickness. This could be an indication that prominence structures at the altitudes in question would not be expected to be at 8000 *K*, however the C2D2E code may have converged too early, or too many approximations were made during the calculations which followed the initial C2D2E results. Due to time constraints, a solution for the issue has currently not been resolved.

Figure 4.5 shows the results for integrated intensity of the D₃ emission as a function of temperature for two different altitudes and two different gas pressures. The general shape of the graph closely follows the results published in previous papers [10, 16], however the intensities of

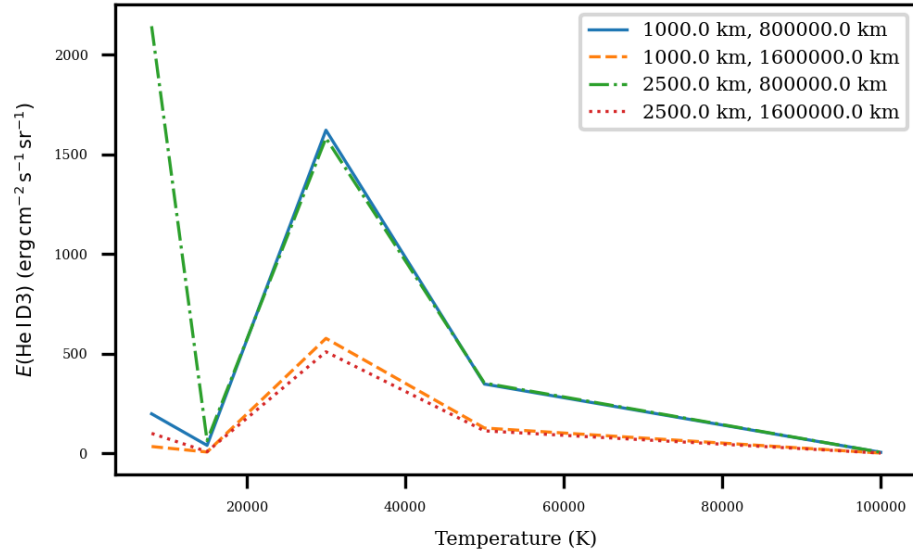
the D₃ line do vary. For example, the intensity of the solid blue line at 30,000 *K* peaks at around 4000 *erg cm⁻² s⁻¹ sr⁻¹*, whereas previous results indicate this intensity would be 2500 *erg cm⁻² s⁻¹ sr⁻¹* at most for the same model [10], as shown previously in figure 1.5. It should also be noted that the previous 1D simulations include intensity contributions from visible light, whereas the current results do not. It is evident that the majority of models exhibit higher integrated intensities than their 1D model counterparts. However, the green dot-dash line displays an uncharacteristic spike in D₃ intensity at 8000 *K*. The reasons for this behaviour requires more time and analysis, hence unfortunately no reason can be given currently. The peak at 30,000 *K* is more interesting when considered alongside the contribution functions shown in figures 4.2, 4.4, 6.1 and 6.2. The PCTR models (table 3.1) had a central region at a temperature of 8000 *K*, with the PCTR being limited to a maximum temperature of 100,000 *K*. The contribution function plots all showed line formation from within a central region of the PCTR, and the maximum intensities shown across figures 4.5 and 4.6a would indicate that this formation region in the PCTR occurs at 30,000 *K*. This suggests that the D₃ emission is not exclusively formed in the central region of a prominence, but rather between the central region and the PCTR.

The results for the helium abundance ratio dependent models, shown in figure 4.6a, produced the expected results. This shows the integrated intensity of the D₃ emission as a function of temperature for two different altitudes and two different helium abundance ratios. They followed the same trend as the pressure dependent models shown in figure 4.5, with a peak in intensity at 30,000 *K* and decrease in intensity as the temperature increased. However, the abundance ratio models were the only models in which the prominence composition parameter, in this case the helium abundance ratio, dominated the altitude in terms of intensity. This is due to the increased probability of collisions and transitions due to the high helium abundance, with the green dash-dot model displaying a huge increase in intensity due to a high helium abundance ratio (0.3) and low altitude (800,000 *km*). As before, this has been caused by the incident radiation from the solar disk included in the C2D2E code. In all other results in this report, and previous referenced 1D results ([10, 16]), there is a clear relationship between the altitude of the prominence and the observed intensity.

With regards to figure 4.6b, this shows the integrated intensity of the D₃ transition as a function of temperature for two different altitudes and two different radii's. As can be seen from figure 4.6b, altering the radius of the cylinder does not have an effect on the integrated intensity. This is most evident at an altitude of 800,000 *km*, where the solid blue line and the green dot-dash produce almost identical emission intensities from 15,000 *K* to 100,000 *K*. From this



(a) Models altering the helium abundance ratio.



(b) Models altering the cylindrical radius.

Figure 4.6: This figure shows the results from models altering the helium abundance ratios (top) and models altering the cylindrical radius (bottom). These models have no PCTR and show integrated intensity of the D₃ emission as a function of temperature. The graph legends show the helium abundance ratio (top) and the cylindrical radius (bottom) alongside the altitude of the model.

plot, it is clear that the radius does not impact the ability for ASPIICS or METIS to observe a prominence structure, although it must be large enough for them to detect initially. The key

point to take is the impact that altitude has on potential measurements, and that prominence structures are more observable the closer they are to the sun due to the increase in intensity from the D₃ emission.

Additionally, for both the abundance ratio and cylindrical radius plots, uncharacteristic intensity spikes occur at a temperature of 8000 *K*. Again, the cause for this behaviour is unknown, and time limitations caused any investigation into the reason of this effect to be beyond the scope of this project. What makes this occurrence strange is the fact that only one model per plot displayed this behaviour, as the remaining models followed the expected pattern. Further analysis must be done to discover why this occurs, and if it is indeed correct.

Chapter 5

Conclusions

In conclusion, this project provided new insights into the D_3 transition by using the C2D2E cylindrical radiative transfer code to run new simulations. First, it looked at different forms of the emission measure as a function of the integrated intensity of the D_3 line using PCTR models in which the helium abundance ratio was changed. For these results, the contribution function was generated for three different abundance ratio models to assess where the main bulk of the D_3 emission was originating from in the cylinder. Then, models which altered the cylindrical radius were used, the emission measures analysed, and the contribution function generated to perform the same analysis. This was a continuation of previous work by Dr. Andrew Rodger [31] to assess the diagnostic potential of the emission measure. Finally, new non-PCTR models which looked at the effects of gas pressure were simulated, which mirrored previous 1D simulations [10, 16], with the aim of assessing the conclusions of the 1D models in terms of the new 2D simulations. Expanding on these comparisons, non-PCTR abundance ratio and cylindrical radius models were also shown. The information from these models can then be applied to ASPIICS and METIS to aid their search for solar prominence events and help provide a deeper understanding of how prominence structures are formed and develop over time.

To summarise, the results of the models with a PCTR pointed towards gas pressure having a significant role within a prominence. By looking at the emission measures as a function of the integrated intensity of the D_3 emission for models with a changing helium abundance ratio, it was found that these pushed the model dependent increases in emission measure closer together when compared to the gas pressure dependent models in previous work [31]. The contribution function for the abundance ratio models showed that, whilst the majority of line formation does take place at the centre of the prominence, some formation does take place in the PCTR due to

the strong ring structure displayed across all three models. As the abundance ratio increases, the line formation at the centre of the prominence begins to show a sensitivity towards the bottom of the cylinder, caused by the incident radiation from the solar disk instigating more collisions and atomic transitions. It was proposed that the ionization of He I atoms, followed by the recombination of He II atoms, may also contribute to this effect, however more research into this area is required. Again, for the models varying the cylindrical radius, the model dependent increases seen in the majority of the emission measures as a function of D_3 integrated intensity are much more orderly than the previously analysed models which varied the gas pressure. This was caused by the changing line-of-sight value due to the nature of the models. For both sets of models, the electron-singly-ionized helium emission measure maintained a linear relationship, which allows for the possibility of extracting diagnostic information. For example, it is possible to measure the density of singly-ionized helium if the electron density can be estimated, and measurements of the line of sight and the intensity of the D_3 line were known. The contribution functions for the models changing the cylindrical radius indicated strong line formation originating from the centre of the prominence and the PCTR. This is seen mostly in the model with a 2000 km radius, which indicates that the majority of the line formation comes from the PCTR.

With regards to the non-PCTR models, these results followed the same pattern as previous results [10, 16], with a peak in integrated intensity of the D_3 line as a function of temperature at a temperature of 30,000 K . During the initial calculations, it was found that some models at a temperature of 8000 K were displaying a negative optical thickness, however all models were included in the final results. Whilst displaying the same general behaviour, the model with a gas pressure of 0.1 $dyn\ cm^{-2}$ and an altitude of 800,000 km produced a greater integrated intensity at a temperature of 30,000 K than previous studies. This indicates that the D_3 emission might be easier to detect by ASPIICS and METIS than previously anticipated. Furthermore, it was suggested that the peak seen at a temperature of 30,000 K may potentially be the region causing the line formation seen in the PCTR, as this trend is consistent across all non-PCTR models. The models which varied the abundance ratio produced the expected results and showed that a prominence with a greater helium abundance ratio will produce a greater integrated intensity. These were the only models in which both values of the parameter being studied, in this case the helium abundance ratio, produced a greater D_3 intensity than the models at an altitude of 800,000 km . Finally, the models evaluating the effects of altering the cylindrical radius produced an interesting conclusion. Due to the close proximity of the two models at an altitude of 800,000 km models and the two models at an altitude of 1,600,00 km models, it was concluded that the radius of the cylinder does not have an impact on the results, and the altitude of the

cylinder has a far greater effect on the intensity of the D_3 transition.

For the continuation of this project, there are various avenues which new research can take. Initially, it is important to diagnose the reason for the intensity spikes seen at a temperature of 8000 K in the non-PCTR models, and whether this is the result of a genuine 2D effect. Once resolved, one could pursue the avenue of analysing the magnetic structure of the emissions from the non-PCTR models, to see if any 2D effects occur when measuring the linear polarization. More data points could also be introduced, as this could give a better insight into the behaviour of the plots. With regards to the PCTR models, further analysis could be conducted by changing the parameters to align with the non-PCTR models, which could provide analysis on PCTR related effects. Similarly, it would be interesting to see if the intensity spike at a temperature of 30,000 K does align with the contribution function of these new models and may prove that 30,000 K is a significant formation region for the D_3 line within the PCTR. Finally, it should be established whether the calculations can track the D_3 emission as it progresses through the PCTR, as this would provide an excellent amount of data points to plot integrated intensity against temperature and show how the PCTR influences the intensities observed, similar to how the contribution function tracks the D_3 integrated intensity with respect to the position in the cylinder. The research conducted within the duration of this project will contribute to future prominence research, and within time (and pending the observed results of the space-based missions discussed) the nature of a prominence event will be well understood.

Chapter 6

Appendix

6.1 D3 Contribution Function & 584 Å Contribution Function

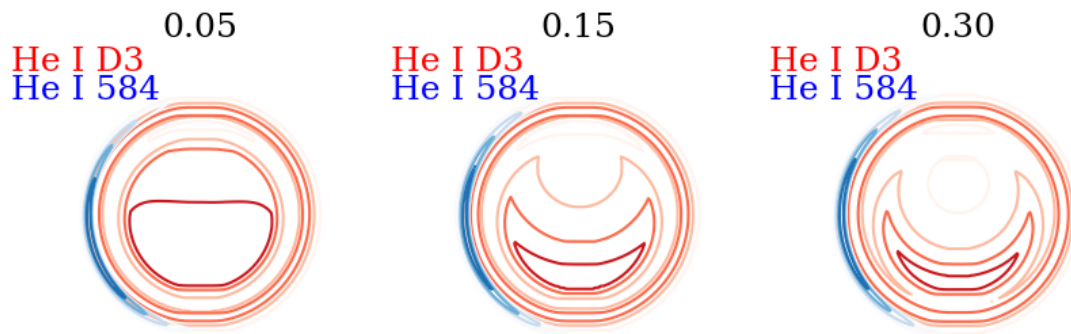


Figure 6.1: Contribution Function plotting the evolution of the intensity from D3 and 584 Å for the abundance ratio models in table 3.1. This gives an idea of where the D3 line is formed, since the optically thick 584 Å line is formed exclusively in the PCTR.

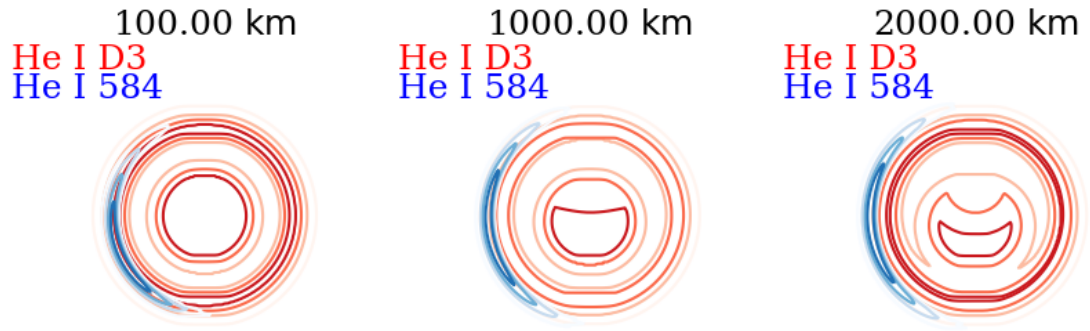


Figure 6.2: Contribution Function plotting the evolution of the intensity of the D3 and 584 Å lines models altering the cylindrical radius in table 3.1.

Chapter 7

Bibliography

- [1] European Space Agency. About PROBA-3. *esa.int/Proba_Missions/About_Proba-3*, (Last Accessed: 03.07.2020).
- [2] European Space Agency. Solar orbiter. *esa.int/Science_Exploration/Space_Science/Solar_Orbiter*, (Last Accessed: 03.07.2020).
- [3] E. Antonucci *et al.* Metis: The solar orbiter visible light and ultraviolet coronal imager. *Astronomy & Astrophysics*, (35338):42, 2019.
- [4] M. Asplund, N. Grevesse, A. Jacques Sauval, and P. Scott. The chemical composition of the sun. *Annual Review of Astronomy & Astrophysics*, :481:522, 2009.
- [5] V. Bommier, J. L. Leroy, and S. Sahal-Brechot. Determination of the complete vector magnetic field in solar prominences using the Hanle effect. *Astronomy & Astrophysics*, **100**:231–240, 1981.
- [6] R. Casini, A. López Ariste, S. Tomczyk, and B. W. Lites. Magnetic maps of prominences from full stokes analysis of the He I *D*3 line. *The Astrophysical Journal*, **598**:L67–L70, 2003.
- [7] M Chane-Yook. C2d2e: Non-LTE 2D radiative transfer in cylindrical threads with incident radiation (hydrogen + helium). *C2D2E User Guide, IDOC*, :25, 2009.
- [8] G. Del Zanna, P. J. Storey, N. R. Badnell, and V. Andretta. Helium line emissivities in the solar corona. *The Astrophysics Journal*, **898**(1), 2020.
- [9] P. Demoulin. Magnetic fields in filaments. *New Perspectives on Solar Prominences*, **150**:IAU Colloquium 167, 1998.

- [10] S. Fineschi et al. Optical design of the multi-wavelength imaging coronagraph METIS for the solar orbiter mission. *Experimental Astronomy*, **49**:239–263, 2020.
- [11] P. Gouttebroze. Radiative transfer in cylindrical threads with incident radiation. II. 2D azimuth-dependent case. *Astronomy & Astrophysics*, **434**:1165–1171, 2005.
- [12] P. Gouttebroze, P. Heinzel, and J. C. Vial. The hydrogen spectrum of solar prominences. *Astronomy & Astrophysics*, **99**(3):513–543, 1993.
- [13] P. Gouttebroze and N. Labrosse. A ready-made code for the computation of prominence NLTE models. *Solar Physics*, **96**:349–355, 2000.
- [14] P. Gouttebroze and N. Labrosse. Radiative transfer in cylindrical threads with incident radiation. VI. A hydrogen plus helium system. *Astronomy & Astrophysics*, **503**:663–671, 2009.
- [15] P. Heinzel *et al.* On the possibilities of detecting helium D₃ line polarization with METIS. *The Astrophysical Journal*, 2020.
- [16] S. Ježić, P. Heinzel, N. Labrosse, A. N. Zhukov, A. Bemporad, S. Fineschi, and S. Gunár. Visibility of prominences using the He I D₃ line filter on PROBA-3/ASPIICS coronagraph. *Solar Physics*, **293**(33), 2018.
- [17] N. Labrosse and P. Gouttebroze. Formation of helium spectrum in solar quiescent prominences. *Astronomy & Astrophysics*, **380**:323–340, 2001.
- [18] N. Labrosse and P. Gouttebroze. Non-LTE radiative transfer in model prominences. I. Integrated intensities of He I triplet lines. *The Astrophysical Journal*, **617**:614–622, 2004.
- [19] N. Labrosse, P. Gouttebroze, P. Heinzel, and J. C. Vial. Line profiles and intensity ratios in prominence models with a prominence to corona interface. *Solar variability: from core to outer frontiers. The 10th European Solar Physics Meeting*, **1**:451–454, 2002.
- [20] N. Labrosse, P. Heinzel, J. C. Vial, T. Kuncera, S. Parenti, S. Gunár, B. Schmieder, and G. Kilper. Physics of solar prominences: I - spectral diagnostics and non-LTE modelling. *Space Science Reviews*, **151**:39–78, 2010.
- [21] L. Léger and F. Paletou. 2D non-LTE radiative modelling of He I spectral lines formed in solar prominences. *Astronomy & Astrophysics*, **498**:869–875, 2009.
- [22] K. Lodders. Solar system abundances and condensation temperatures of the elements. *The Astrophysical Journal*, **591**:1220–1247, 2003.

- [23] A. López Ariste. Instrument concepts for the observation of prominences with future ground-based telescopes. *Nature of prominences and their role in space weather*, **Proceedings IAU Symposium**(300), 2013.
- [24] A. López Ariste and R. Casini. Magnetic fields in prominences: Inversion techniques for spectropolarimetric data of the He I D_3 line. *The Astrophysical Journal*, **575**:529–541, 2002.
- [25] A. López Ariste and R. Casini. Improved estimate of the magnetic field in a prominence. *The Astrophysical Journal*, **582**:L51–L54, 2003.
- [26] D. H. MacKay, B. Schmieder, A. López Ariste, and Y. Su. Modelling & observations: Comparison of the magnetic field properties in a prominence. *Astronomy & Astrophysics*, **637**(A3), 2020.
- [27] NASA. Solar prominences. <https://eclipse2017.nasa.gov/solar-prominences>, (Last Accessed: 02.07.2020).
- [28] F. Paletou, A. López Ariste, V. Bommier, and M. Semel. Full-stokes spectropolarimetry of solar prominences. *Astronomy & Astrophysics*, **375**:L39–L42, 2001.
- [29] C. W. Querfeld, R. N. Smartt, V. Bommier, E. L. Degl’innocenti, and L. L. House. Vector magnetic fields in prominences. II. He I D_3 Stokes profiles analysis for two quiescent prominences. *Solar Physics*, **96**:277–292, 1985.
- [30] E. Renotte et al. Design status of ASPIICS, an externally occulted coronagraph for PROBA-3. *SPIE Proceedings Conference*, **9604**, 2015.
- [31] A. Rodger. Millimetre-continuum diagnostics and non-LTE radiative transfer modelling of solar prominences. *PhD Thesis, The University of Glasgow*, , 2019.
- [32] R. J. Rutten. An introduction to solar spectrum formation. *National Solar Observatory/Sacramento Peak Summer Course*, :21–33, 1993.
- [33] R. J. Rutten. Radiative transfer in stellar atmospheres. *Utrecht University lecture notes*, (8th edition), 2003.
- [34] B. Schmieder, A. López Ariste, P. Levens, N. Labrosse, and K. Dalmasse. Polarimetric measurements in prominences and “tornadoes” observed by THEMIS. *Polarimetry: From the Sun to Stars and Stellar Environments*, **Proceedings IAU Symposium**(35):275–281, 2014.

- [35] B. Schmieder et al. Open questions on prominences from co-ordinated observations by IRIS, Hinode, SDO/AIA, THEMIS, and the Meudon/MSDP. *Astronomy & Astrophysics*, **569**(A85), 2014.
- [36] J. C. Vial et al. Solar prominences. *Astrophysics and Space Science Library*, **First Edition**:103–157, 2015.
- [37] V. Vrsnak. Eruptive instability of cylindrical prominences. *Solar Physics*, **129**:295–312, 1990.